Science
AAAS

# Supplementary Materials for

## Recent global temperature surge intensified by record-low planetary albedo

Helge F. Goessling, Thomas Rackow, Thomas Jung

Corresponding author: Helge F. Goessling, helge.goessling@awi.de

DOI: 10.1126/science.adq7280

**The PDF file includes:**

## Materials and Methods

Data

We use three public datasets to explore Earth's energy budget, surface temperature and clouds, namely (i) the Clouds and the Earth's Radiant Energy System (CERES) Energy Balanced and Filled (EBAF) Top-of-Atmosphere (TOA) Edition-4.2 Data Product from the US National Aeronautics and Space Administration (NASA; *14*, hereafter CERES), (ii) the ERA5 reanalysis produced by the European Centre for Medium-Range Weather Forecasts (ECMWF; *17*, *18*), and the Ocean Niño 3.4 Index (ONI) produced by the US National Oceanic and Atmospheric Administration (NOAA).

CERES is a satellite-based product intended to provide a long-term record for detecting decadal changes in Earth's global radiation budget, clouds and aerosols (*14*). Besides measurements of radiation emitted from Earth, the CERES-EBAF product also includes measurements of TOA incident solar radiation based on a composite out of multiple data records (*16*). CERES includes a one-time adjustment of the TOA fluxes to ensure that the global-mean net TOA flux for July 2005–June 2015 is consistent with an in-situ value of 0.71 $Wm^{-2}$. In addition to the monthly TOA all-sky and clear-sky radiation fluxes on a 1-degree longitude-latitude grid, available from March 2000–December 2023, we use the total cloud cover fractions based on the Moderate Resolution Imaging Spectrometer (MODIS) contained in the CERES product (*15*).

ERA5 is ECMWF's latest reanalysis product, updated on a daily basis in near-real-time (*17*, *18*). It combines an extensive set of satellite and in-situ observational data with a fixed version of ECMWF's physical numerical weather prediction model by a sophisticated data assimilation scheme. It thereby provides a gap-free global gridded estimate of the evolution of a large number of variables, including clouds and radiation fluxes, reaching back to January 1940. Long-term trends in ERA5 need to be interpreted with caution due to possible shifts resulting from changes in the observing system, including strongly reduced data density in earlier decades. Moreover, due to the data assimilation, total mass and energy budgets in ERA5 are not closed (17). This implies that absolute values of quantities like the top-of-atmosphere total imbalance (EEI) are spurious. It is thus important to consider anomalies, like we do throughout this work, rather than absolute values.

Given that CERES data is also subject to uncertainties, we use ERA5 (i) as an additional data product, even though not fully independent as the satellite data sources are overlapping, (ii) to get some evidence for the evolution of relevant parameters before March 2000, keeping in mind the possibility of spurious trends, and (iii) to analyze the height-dependence of cloud changes based on three categories, namely low-level (atmospheric pressure above about 800hPa), mid-level (atmospheric pressure between about 800hPa and 450hPa), and high-level (atmospheric pressure below about 450hPa) clouds. For consistency, all monthly ERA5 data has been remapped from the original 0.28-degree grid to the 1-degree CERES grid by first-order conservative remapping prior to analysis.

Total cloud cover is about 4-5% lower in ERA5, although this may be due to differences in cloud definitions rather than being an actual bias. Apart from that, global-mean ERA5 and CERES climatologies are matching rather closely (Fig. S1). Generally, spatio-temporal variations are consistent between the datasets, as visible in numerous figures in this study, suggesting that ERA5 is suitable for the purposes listed above. A notable exception is the TOA incident solar radiation (ISR) where the forcing data in ERA5 starts to diverge from the

observation-based CERES values in 2020. The reason is that ERA5 ISR is based on reconstructed/observed data only until 2008 and assumes a perpetual repetition of the last solar cycle thereafter (*17*). Similarly, sulfate aerosols in ERA5 follow CMIP5 historical and scenario forcings, although based on historical emission estimates until 2009 and scenario data thereafter (*17*).

The NOAA Niño 3.4 index is constructed from 3-month running means of ERSST.v5 sea-surface temperature anomalies in the Niño 3.4 region (5S–5N, 170W–120W), based on centered 30-year base periods updated every 5 years (*28*).

Temperature, cloud and albedo signatures of El Niño

El Niño is a key driver of inter-annual climate variability (*25, 27*). Given that conditions in 2023 transitioned from La Niña to El Niño (Fig. 2b), we estimate the impact of El Niño on temperatures, radiation fluxes and clouds in 2023 based on previous El Niño events. We consider a set of the 4 pre-2023 El Niño events covered by the CERES period (2002/03, 2006/07, 2009/10, 2015/16) based on CERES and ERA5 data, and an extended set of 9 pre-2023 El Niño events (1951/52, 1957/58, 1968/69, 1972/73, 1997/98, 2002/03, 2006/07, 2009/10, 2015/16) based on ERA5 data. Events influenced by volcanic eruptions and the double-event 1987/88 (Fig. S3) are excluded. To isolate anomalies associated only with El Niño, anomalies for each event have been normalized by subtracting the average anomalies of the two years flanking each event, that is, the year before the El Niño onset year and the year after the El Niño second year. Nonlinear longer-term trends, including seasonally-varying ones, are thereby removed. We consider multi-event composites to estimate the temporal evolution of several parameters over the course of an average event (Fig. S7), including the shortwave signature, and individual events to estimate the temperature anomaly due to El-Niño in 2023 (Fig. S8). Given that 2023 was an El Niño onset year, the main focus is on these.

During El Niño, warmer ocean surface waters are exposed in the eastern tropical Pacific by internal redistribution of water masses (*27*; Fig. S7g), resulting in higher global-mean surface temperature (Figs. 2a,b,S7a). During previous events, the normalized annual-mean GMST anomaly during El Niño onset years was mostly around +0.05K to +0.10K, with a dependence on the annual-mean Niño 3.4 index (Fig. S8). Based on the 2023-mean Niño 3.4 index anomaly and linear least-squares regression, we estimate that El Niño has contributed about +0.07(±0.04)K (90% confidence interval) to the 2023 temperature anomaly.

Modulated by a complex interplay of different energy fluxes and mechanisms, the surface warming associated with El Niño leads to increased global-mean TOA outgoing longwave radiation. This results in a decreased total imbalance (EEI) (Fig. S7b, consistent with *25*), although modified by a total absorbed solar radiation (ASR) signature (Fig. S7c,h) and hence a planetary albedo signature (Fig. S7d) related mainly to cloud patterns (Fig. S7e,f,i,j) (*24, 25, 26*). Based on the ERA5-based nine-event composite, the global and annual-mean ASR signature during El Niño onset years is +0.08(±0.06)$Wm^{-2}$ (planetary albedo about -0.02%; dashed curves in Fig. S7c,d) and thus only a small fraction of the total 2023 ASR anomaly of +1.82$Wm^{-2}$ in CERES and +1.33$Wm^{-2}$ in ERA5. The contribution of the El Niño albedo signature to the 2023 GMST anomaly is about an order of magnitude smaller compared to the general temperature signature of +0.07(±0.04)K (see above). The possible ASR

contribution of El Niño is thus not treated separately in counterfactuals based on the energy balance model integrations (see below).

Empirical estimation of total cloud cover-inferred ASR anomalies

To estimate the contribution of total cloud cover (TCC) changes to the ASR anomalies and trends, we have fitted power functions of the form

(1) $CRE = \alpha \cdot TCC^{\beta}$

to the monthly-mean TCC and shortwave cloud radiative effect (CRE) data for each of the 1-degree grid points for each calendar month and dataset separately. To keep the parameters within physically reasonable bounds even where the TOA incident solar radiation is very small or CRE variations are strongly confounded by surface albedo variations, we bounded $\alpha$ within [-ISR,ISR] and $\beta$ within [1,4]. We have used only the inter-annual variations within 2001–2014, because during this period global-mean ASR and low-cloud cover were still relatively stationary (Fig. 2d,f) and in order to exclude any potential aerosol-cloud effects that might have been caused by the two IMO regulation changes in 2015 and 2020. Given the small sample size, for each grid point we have also included the data of neighboring grid cells within 2 degrees in meridional and zonal direction, as long as the climatological surface albedo differs by at most 5%.

Results of fitted parameters and explained variance are shown exemplarily for May in Fig. S9. The fitted power functions have subsequently been used to infer a hypothetical CRE going back to TCC-anomalies alone, termed CREtc (Figs. 2d,S1f,S4b,d,S5c,d,S6c,d, Tab. 1). CREtc accounts not only for an isolated cloud amount effect, where CRE is proportional to TCC (*34*), but also for changes in CRE through covariances between TCC and cloud optical depth and altitude. We find that, arguably due to these covariances, cloud radiative effect typically depends superlinearly on total cloud cover in both datasets (Fig. S9c,d), with regional differences that may be related to the dependence of cloud overlap on cloud regimes.

2-layer energy balance model and ASR-based counterfactuals

The 2-layer energy balance model (EBM) used in this study to estimate temperature responses to absorbed solar radiation (ASR) anomalies follows earlier work by (*43*) and (*44*). The EBM adopted here splits the Earth system into two main layers. It describes the evolution of upper-layer temperature perturbations $T$ and a deep-ocean layer temperature perturbation $T_0$ over time as a system of two ordinary differential equations (ODEs)

(2) $C\frac{dT(t)}{dt} = F(t) - \lambda T(t) - \gamma(T(t) - T_0(t))$

(3) $C_0\frac{dT_0(t)}{dt} = \gamma(T(t) - T_0(t))$ ,

where $C$ is a heat capacity for the atmosphere-land-upper-ocean system; $F$ is a radiative forcing amplitude function that may vary over time, $t$; $\lambda$ is the radiative feedback parameter

for a $CO_2$ perturbation; $\gamma$ is an exchange coefficient between the upper and deeper ocean layers; and $C_0$ is the deep-ocean heat capacity. The parameters of the EBM follow Tables 3 and 4 in (*44*), where parameter fits to CMIP5 models are presented. For our central estimates we use the CMIP5 multi-model mean (MMM, based on 15 models) for the individual parameters, as repeated for convenience in Table S1. In addition, we use the sets of parameters corresponding to each of the CMIP5 models individually to derive uncertainties for the estimated temperature response contributions (see next section). Solar forcing is less effective than an equivalent $CO_2$ forcing, with an efficacy of $F_{eff} = 92\%$ (*42*). Originally this estimate is for ASR anomalies due to solar intensity anomalies rather than planetary albedo anomalies, but we assume that it holds for the latter, too. We thus multiply by this factor in $F$ when using ASR anomalies from ERA5 or CERES as input to the EBM.

Another way to look at the system of equations is that the left-hand sides of the ODEs describe the tendencies of upper-layer (Eq. 2) and deep-layer (Eq. 3) heat contents (*44*). The chosen MMM value for the upper-layer $C$ heat content roughly implies an effective mixed layer thickness of 77m (*44*). With the chosen mean values, the upper and deeper ocean layers respond on a timescale of 4.1 years and 219 years, respectively (*44*).

The 2-layer EBM has simple analytical solutions for linear and step-wise forcing functions $F$ (*44*). In our implementation, the system of ODEs is solved numerically with a Forward Euler discretisation and monthly timesteps. For a simple step-wise forcing, our numerical solution agrees with the analytical solutions given by (*44*). The EBM returns monthly $T$, $T_0$, and Earth Energy Imbalance (EEI), $F - \lambda T$, as output.

To construct ASR-based counterfactuals where ASR anomalies are assumed to be zero from some time onward, we drive the EBM with monthly CERES and ERA5 ASR anomalies relative to 2001–2022 until December 2023, starting in December each year from 2001 to 2022 (Figs. S10,S11). Subtracting the EBM upper-layer temperature response from the observed GMST provides counterfactuals of how GMST may have evolved without the ASR anomalies. Counterfactuals of the imbalance (EEI) are constructed in the same way. Considering only the shortwave perturbations is reasonable given that the planetary albedo decline is associated primarily with low-level clouds, which lack the compensating longwave effects of mid- and high-level clouds (*45*). We focus on the counterfactuals starting December 2020 because that was about the last time when ASR anomalies in satellite data were close to zero and when the clearest low-cloud and ASR trends set in (Fig. 2d,f).

Additional counterfactuals are constructed by separately using the contributions to the global-mean ASR anomalies (i) from five different zonal bands (Antarctic 90S–55S; Southern mid-latitudes 55S–23S; Tropics 23S–23N; Northern mid-latitudes 23N–55N; Arctic 55N–90N) and (ii) from anomalies of the TOA incident solar radiation (Fig. S2f) by multiplication with the spatio-temporal pattern of absolute planetary albedo. Case (i) also serves to approximate the contribution of surface albedo trends to the global planetary albedo trend. This is reasonable because, first, surface albedo trends are dominated by sea-ice and snow retreat poleward of 55S and 55N and, second, surface albedo trends dominate total planetary albedo trends there.

Uncertainty estimation

All uncertainty estimates provided in this study correspond to 90% confidence intervals. The exact methods and assumptions necessarily differ for different estimates as follows.

The 2023 GMST increase above pre-industrial, referred to as "almost 1.5K" and "close to 1.5K" in the abstract and main text, is relative to 1850—1900, following the C3S and WMO standard based on IPCC AR5 and AR6 (*2*). The uncertainty of the contemporary warming is primarily related to the uncertainty associated with the pre-industrial level, which is about ±0.06K (width of 90% confidence interval) according to C3S (*2*). GMST warming estimates for 2023 from different datasets, provided by C3S (*2*), are: 1.483K (ERA5), 1.468K (JRA-3Q), 1.446K (Berkeley Earth), 1.436K (GISTEMP), 1.438K (HadCRUT5), and 1.443K (NOAAGlobalTemp). In Fig. 1 and for the computation of the uncertainty associated with the "residual warming" (see below) we use the (rounded) ERA5 estimate of +1.48(±0.06)K, including the broader uncertainty estimate from C3S (*2*). Regarding the question by how much the 2023 GMST was above the previous annual record, which was 2016 according to all datasets, the range of estimates is: 0.168K (ERA5), 0.152K (JRA-3Q), 0.167K (Berkeley Earth), 0.152K (GISTEMP), 0.170K (HadCRUT5), and 0.158K (NOAAGlobalTemp). For consistency, in the abstract we refer to the (rounded) ERA5 estimate of "about 0.17K".

For the ASR signature of the El-Niño onset (+0.08(±0.06)W/m$^2$), the half-width of the 90% confidence interval is based on the standard error of the annual-mean ASR of the nine previous El-Niño onset years contributing to the composite, individually normalized as described above. The standard error is multiplied by the 95% quantile of a normal distribution with zero mean and unit standard deviation (≈1.645).

The confidence interval for the GMST anomaly associated with El Niño onset years (+0.07(±0.04)K), derived from the nine previous El Niño onset years (Fig. S8), is the 90% confidence interval of the linear least-squares regression used to predict the annual-mean GMST anomaly from the annual-mean Niño 3.4 index.

A central outcome of this study are the estimates for the 2023 annual-mean GMST response to the various components of the ASR anomalies since December 2020 (see most of the estimates shown in Fig. 1b). For these, the CERES ASR anomalies are considered to be more reliable given the limitations of the ERA5 data outlined above, although the ERA5-based estimates may be regarded as a qualitative indicator of reliability/uncertainty. Like any real-world measurements, also the CERES-based ASR anomalies come with uncertainties, but an accurate quantification of these is beyond the scope of this study. Instead, we have quantified the uncertainty associated with the EBM-based derivation of the 2023 annual-mean GMST response from the ASR anomalies. To this end we have constructed an ensemble of EBMs using parameters fitted to each of the CMIP5 models analyzed in (*44*). Feeding the same

ASR anomalies into each of the EBM variants provides an ensemble of GMST responses. 90% confidence intervals are obtained by multiplying the ensemble standard deviation of the 2023 annual-mean GMST response by the 95% quantile of a normal distribution with zero mean and unit standard deviation (≈1.645).

The uncertainty estimates for the GMST response to ASR anomalies thus reflect the model-based uncertainties of Earth's climate sensitivity and response timescales but do not account for uncertainties associated with the ASR anomalies. We however note that, when removing the global ASR difference between CERES and ERA5 due to the ISR offset to derive the purely albedo-related GMST response, the 90% confidence intervals derived from CERES (+0.22(±0.04)K) versus ERA5 (+0.18(±0.03)K) are consistent. Additional uncertainties arise from the choices made regarding the start date of the ASR-based counterfactuals (December 2020; compare other start dates in Figs. S10,11) and the baseline for the anomalies (2001—2022). These choices were made due to the apparent onset of clear ASR and cloud-cover anomalies around December 2020 and in order to maximize the sample size of the baseline without including the exceptional year of 2023. Still, the GMST response estimates must be regarded as conditional on these choices.

The estimates for the combined marine low-cloud feedback of +0.37(±0.33)W/m$^2$/K and the equilibrium climate sensitivity of 2.3–4.7K correspond to 90% confidence ranges based on (*51*). The latter is taken from (*51*) directly, whereas the low-cloud feedback is the sum of the "Tropical marine low cloud" and the "Middle-latitude marine low-cloud amount" terms (their Tab. 1), with the uncertainty derived by Gaussian error propagation and multiplication by the 95% quantile of a normal distribution with zero mean and unit standard deviation (≈1.645).

Finally, no estimates of statistical significance are provided for the decadal trends shown in this study (Tab. 1, Figs. 4,S5,S6) for the following reasons. It is practically impossible to derive statistical significance of decadal trends in an unambiguous way for climate-related variables given an unknown degree of internal variability across timescales, including multi-decadal. This is already the case for global-mean trends, but even more so for local trends given lower signal-to-noise ratios. For example, decadal trends are strongly influenced by ENSO, as discussed in this study. The problems posed by unknown internal variability cannot be addressed properly by simply taking into account annual-scale autocorrelation when testing for significance of trends, and estimates for annual-scale autocorrelations are highly uncertain given that the CERES data extends over not even 25 years. An additional issue are the uncertainties associated with forced changes, including their temporal nonlinearity. For these reasons we can use the decadal trends reported here only for qualitative evidence, to explore whether the anomalies observed in 2023 may be part of emerging trends. Consistently with this rather qualitative approach aimed at plausibility, we leave the question largely unanswered how much of the trends and anomalies are linked to forced changes (be it with or without feedbacks involved) versus internal variability.

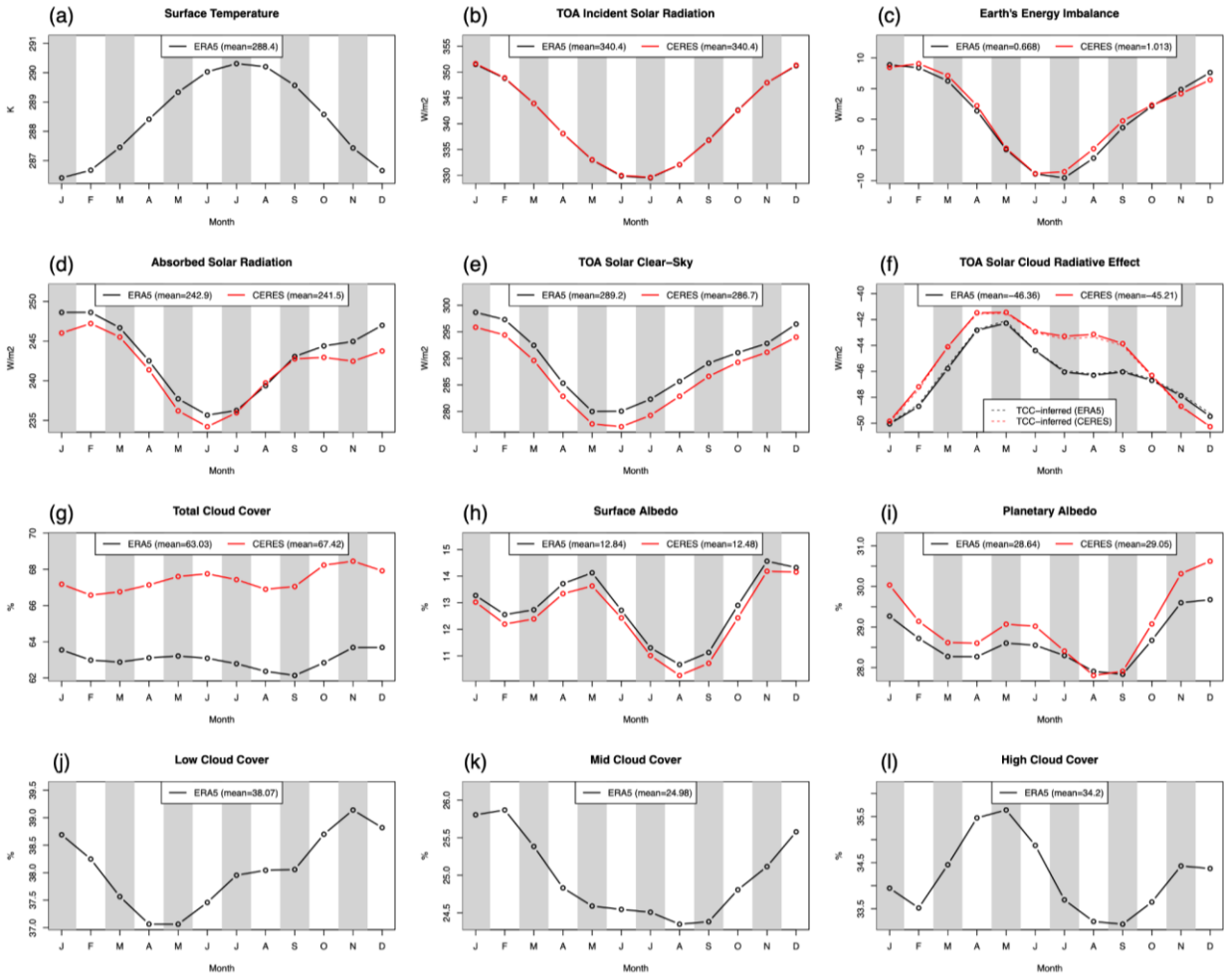


***Fig. S1. Monthly climatologies of relevant quantities related to Earth's energy budget for 2001–2022.*** *(a) Surface (skin) temperature, (b) TOA incident solar radiation (ISR), (c) Earth's TOA total energy imbalance (EEI), (d) TOA net solar radiation (= absorbed solar radiation, ASR), (e) TOA net solar clear-sky radiation, (f) TOA net solar cloud radiative effect (CRE, solid) with values inferred from total cloud cover dashed (CREtc), (g) total cloud cover fraction, (h) surface albedo (derived from global-mean surface solar downwelling and upwelling radiation), (i) planetary albedo (derived from global-mean TOA incident solar and upwelling solar radiation), (j) mid-level cloud cover fraction, (k) mid-level cloud cover fraction, and (l) high-level cloud cover fraction. Red curves show CERES data and black curves show ERA5 data.*

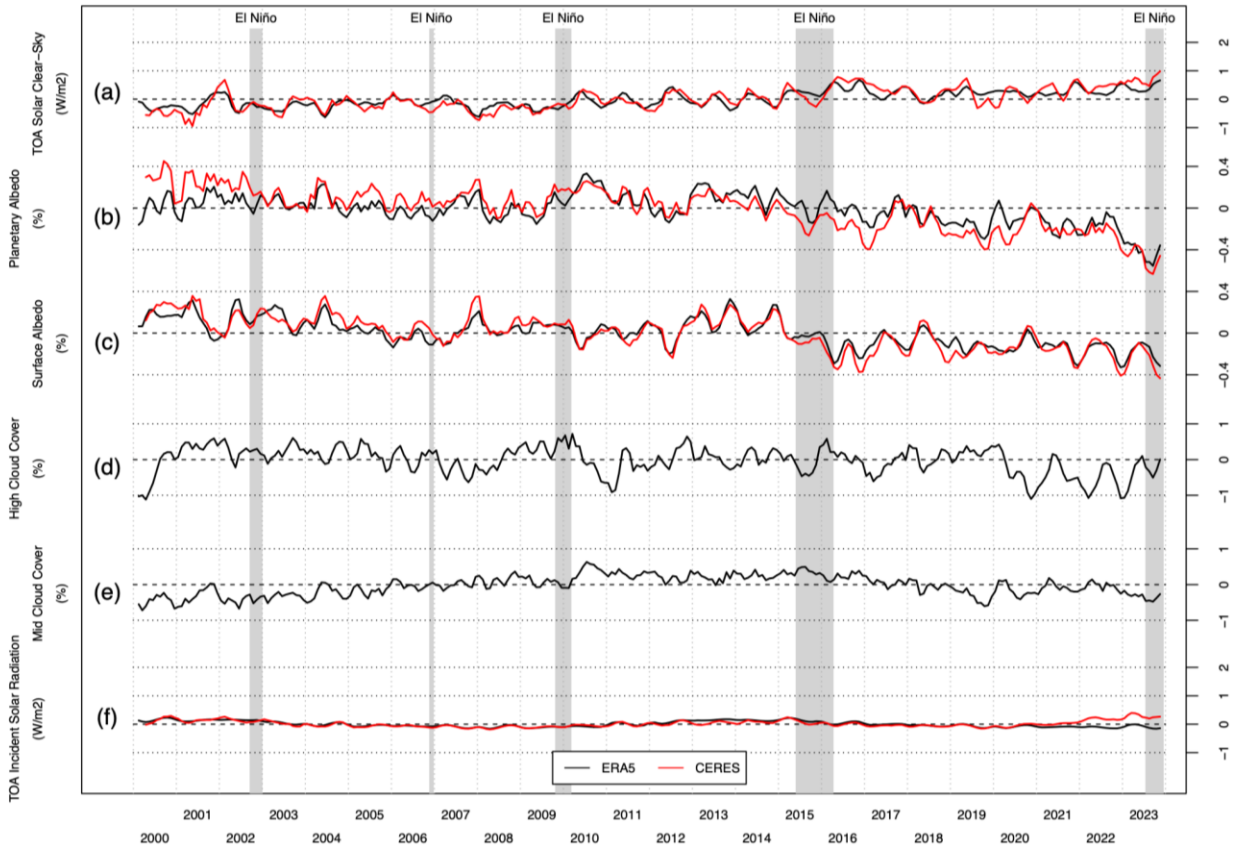


***Fig. S2. Global-mean anomalies of additional quantities related to Earth's energy budget.*** *Three-monthly running-mean anomalies relative to 2001–2022 of (a) TOA net solar clear-sky radiation, (b) planetary albedo (derived from global-mean TOA incident solar and upwelling solar radiation), (c) surface albedo (derived from global-mean surface solar downwelling and upwelling radiation), (d) high-level cloud cover fraction, (e) mid-level cloud cover fraction, and (f) TOA incident solar radiation. Red curves show CERES data and black curves show ERA5 data. El Niño periods with anomalies exceeding +1K (see Fig.1b) are highlighted with gray shading.*

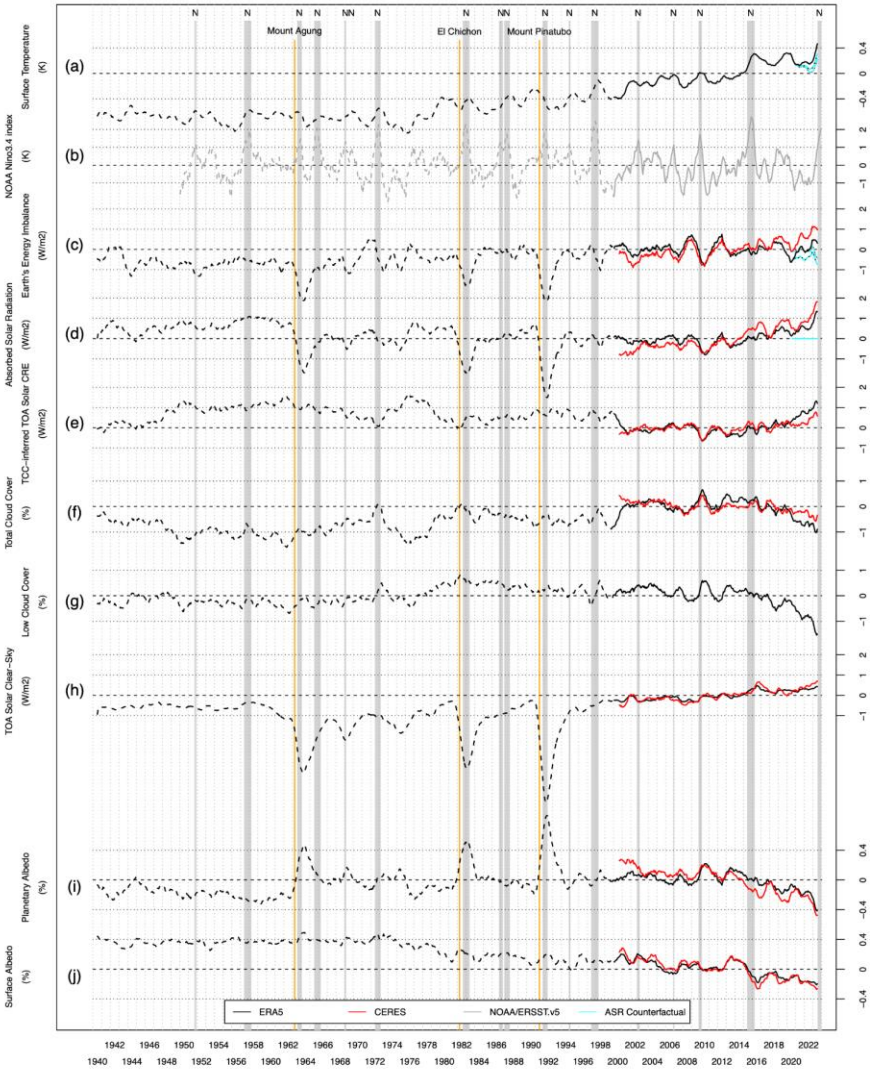


***Fig. S3. Global-mean anomalies of selected quantities related to Earth's energy budget since 1940.*** *Twelve-monthly running-mean anomalies relative to 2001–2022 of (a) surface (skin) temperature, (b) NOAA Ocean Niño 3.4 index, (c) Earth's TOA total energy imbalance, (d) TOA net solar radiation (= absorbed solar radiation, ASR), (e) TOA solar cloud radiative effect inferred from total cloud cover anomalies, (f) total cloud cover fraction, (g) low-level cloud cover fraction, (h) TOA net solar clear-sky radiation, (i) planetary albedo (derived from global-mean TOA solar downwelling and upwelling radiation), and (j) surface albedo (derived from global-mean surface solar downwelling and upwelling radiation). Red curves show CERES data and black curves show ERA5 data. Cyan curves show counterfactuals based on a 2-layer energy balance model where ASR anomalies are assumed to be zero from the beginning of December 2020 onward. El Niño periods with anomalies exceeding +1K are highlighted with gray shading and labeled "N". Curves showing ERA5 data before 2000 are dashed to express that long-term trends can be spurious due to observing-system changes.*

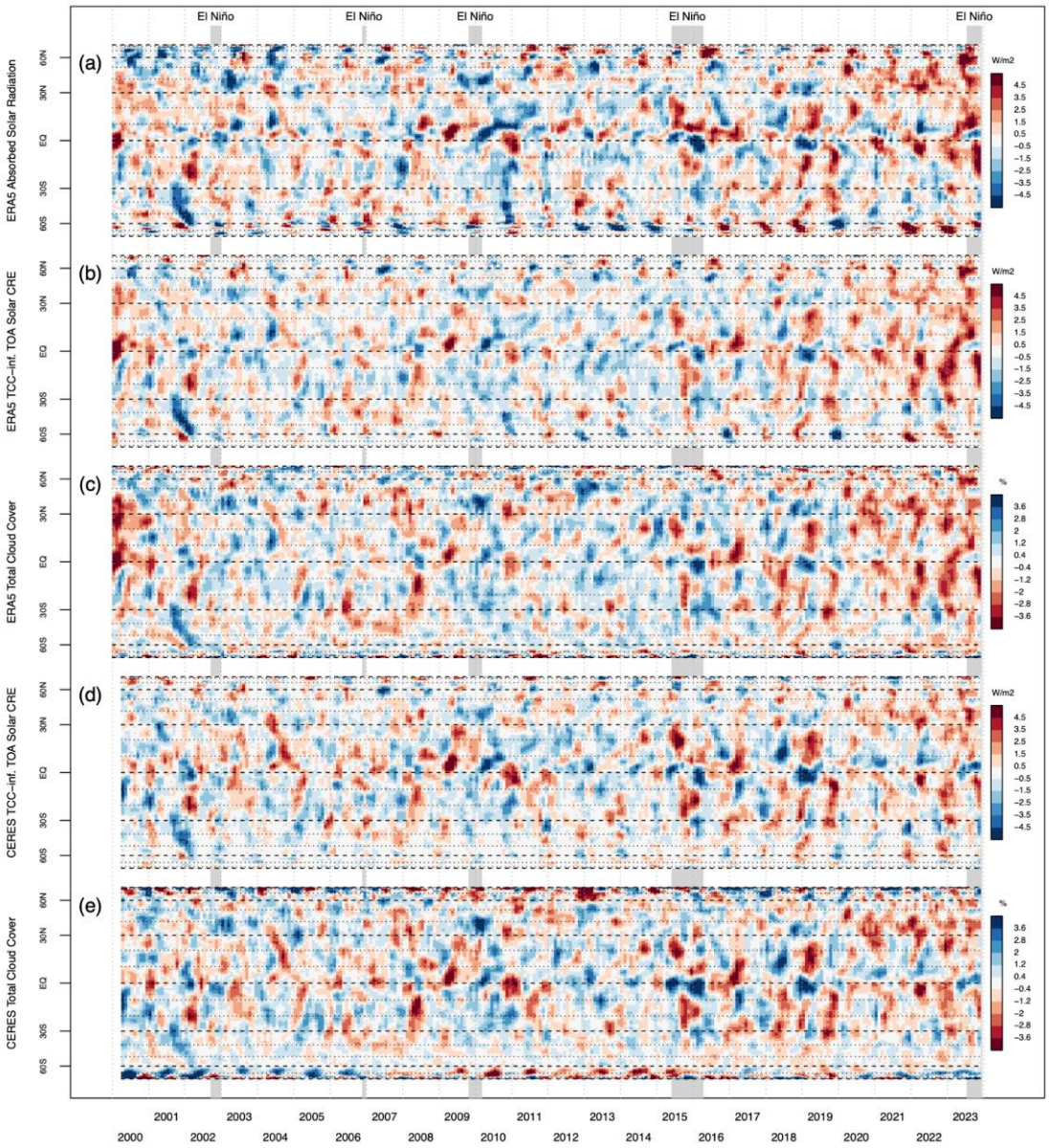


***Fig. S4. Zonal-mean anomalies of additional quantities related to Earth's energy budget.*** *Three-monthly running-mean anomalies relative to 2001–2022 of (a) ERA5 absorbed solar radiation, (b) ERA5 cloud radiative effect inferred from total cloud cover anomalies, (c) ERA5 total cloud cover, (d) CERES TOA solar cloud radiative effect inferred from total cloud cover anomalies, and (e) CERES total cloud cover. El Niño periods with anomalies exceeding +1K are highlighted with gray shading. Latitude spacing corresponds to cosine(latitude) for an equal-area representation.*

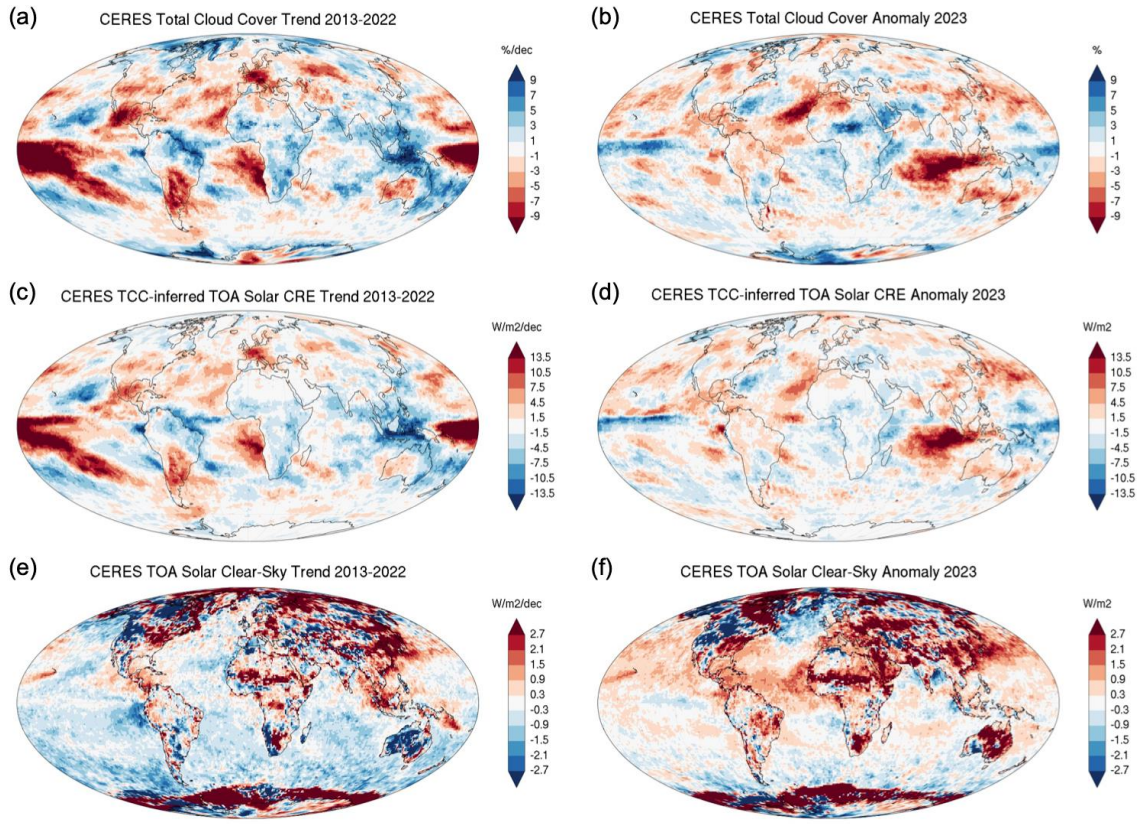


***Fig. S5. Decadal 2013–2022 trends and annual-mean 2023 anomalies of additional parameters related to Earth's energy budget and clouds.*** *CERES trends and anomalies relative to 2001—2022 of (a,b) total cloud cover fraction, (c,d) TOA solar cloud radiative effect inferred from total cloud cover anomalies and (e,f) TOA net solar clear-sky radiation (color scale chosen to resolve anomalies over the open ocean).*

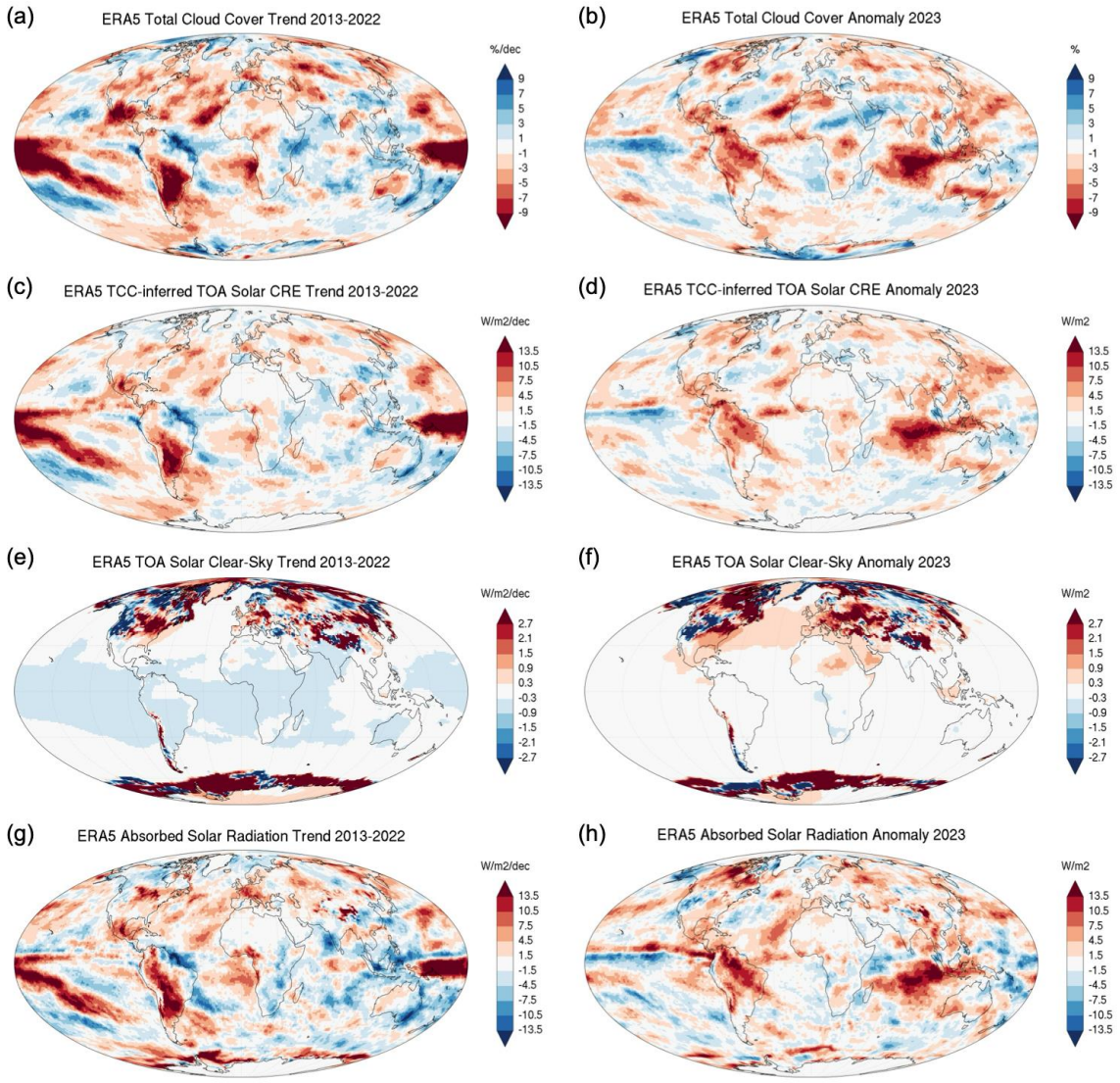


***Fig. S6. Decadal 2013–2022 trends and annual-mean 2023 anomalies of additional parameters related to Earth's energy budget and clouds.*** *ERA5 trends and anomalies relative to 2001—2022 of (a,b) total cloud cover fraction, (c,d) TOA solar cloud radiative effect inferred from total cloud cover anomalies, (e,f) TOA net solar clear-sky radiation (color scale chosen to resolve anomalies over the open ocean) and (g,h) TOA net solar radiation (= absorbed solar radiation, ASR).*

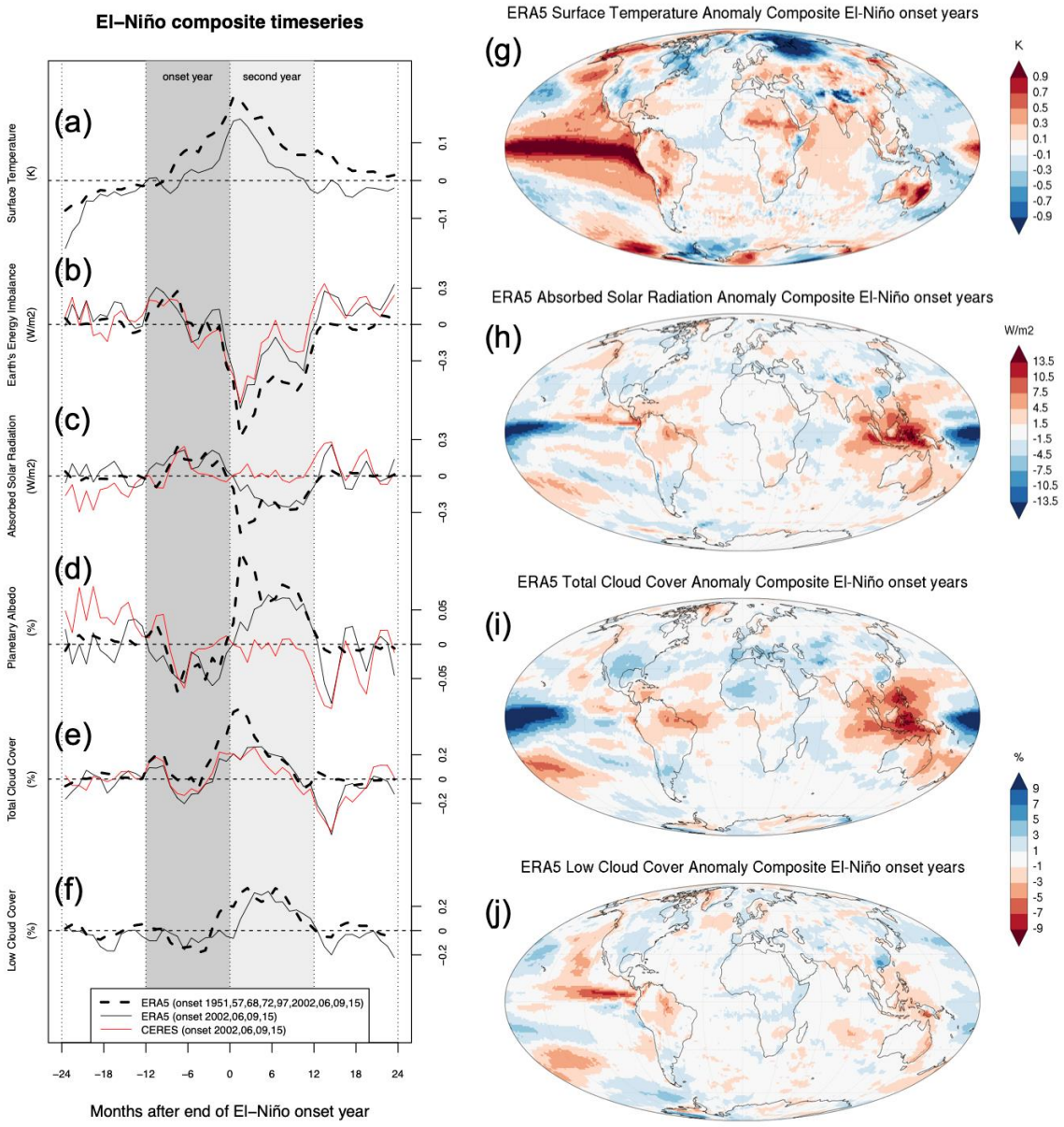


***Fig. S7. El Niño composite analysis.*** *(a-f) Global-mean composites of 4 pre-2023 El Niño events covered by the CERES period based on CERES data (thin solid red curves) and ERA5 data (thin solid black curves) and of an extended set of 9 pre-2023 El Niño events based on ERA5 data (thick dashed black curves) for (a) surface (skin) temperature, (b) Earth's TOA total energy imbalance, (c) TOA net solar radiation (= absorbed solar radiation, ASR), (d) planetary albedo (derived from global-mean TOA solar downwelling and upwelling radiation), (e) total cloud cover fraction, and (f) low-level cloud cover fraction. (g-j) Annual-mean composites of 9 pre-2023 El Niño onset years based on ERA5 data (corresponding to the thick dashed black curves in a-f) for (g) surface (skin) temperature, (h) TOA net solar radiation (= absorbed solar radiation, ASR), (i) total cloud cover fraction, and (j) low-level cloud cover fraction.*

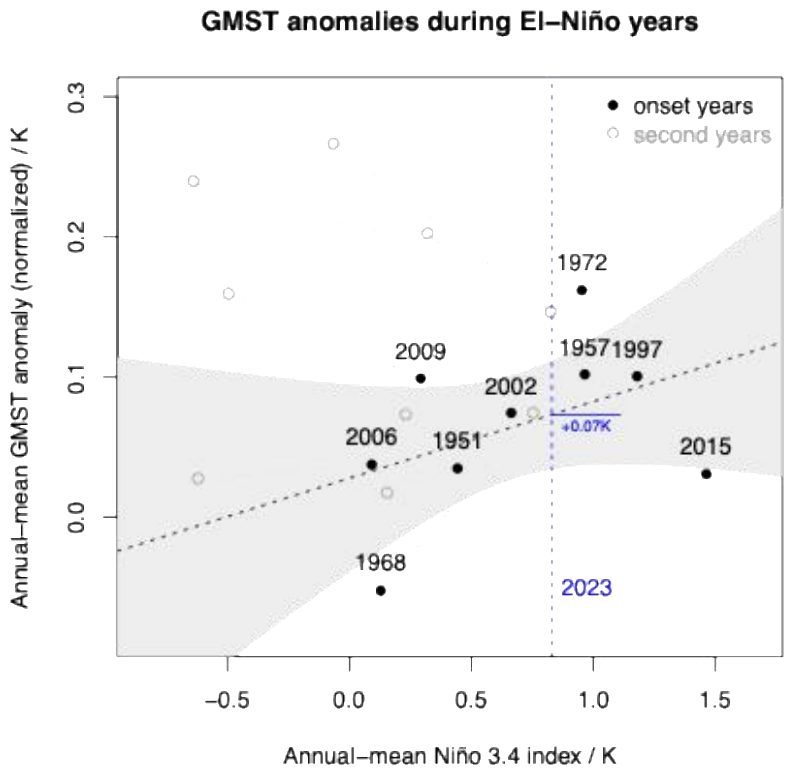


***Fig. S8. Global-mean surface temperature anomalies during El Niño years.*** *Based on annual-means of NOAA Ocean Niño 3.4 index and ERA5 annual-mean surface (skin) temperature for 9 El Niño onset years (black filled circles) and corresponding second years (grey circles). The contribution of El Niño to the 2023 temperature anomaly (+0.07(±0.04)K) is estimated based on the 2023-mean Niño 3.4 index (blue dashed line) with linear least-square regression (black dashed line and 90% confidence band by gray shading).*

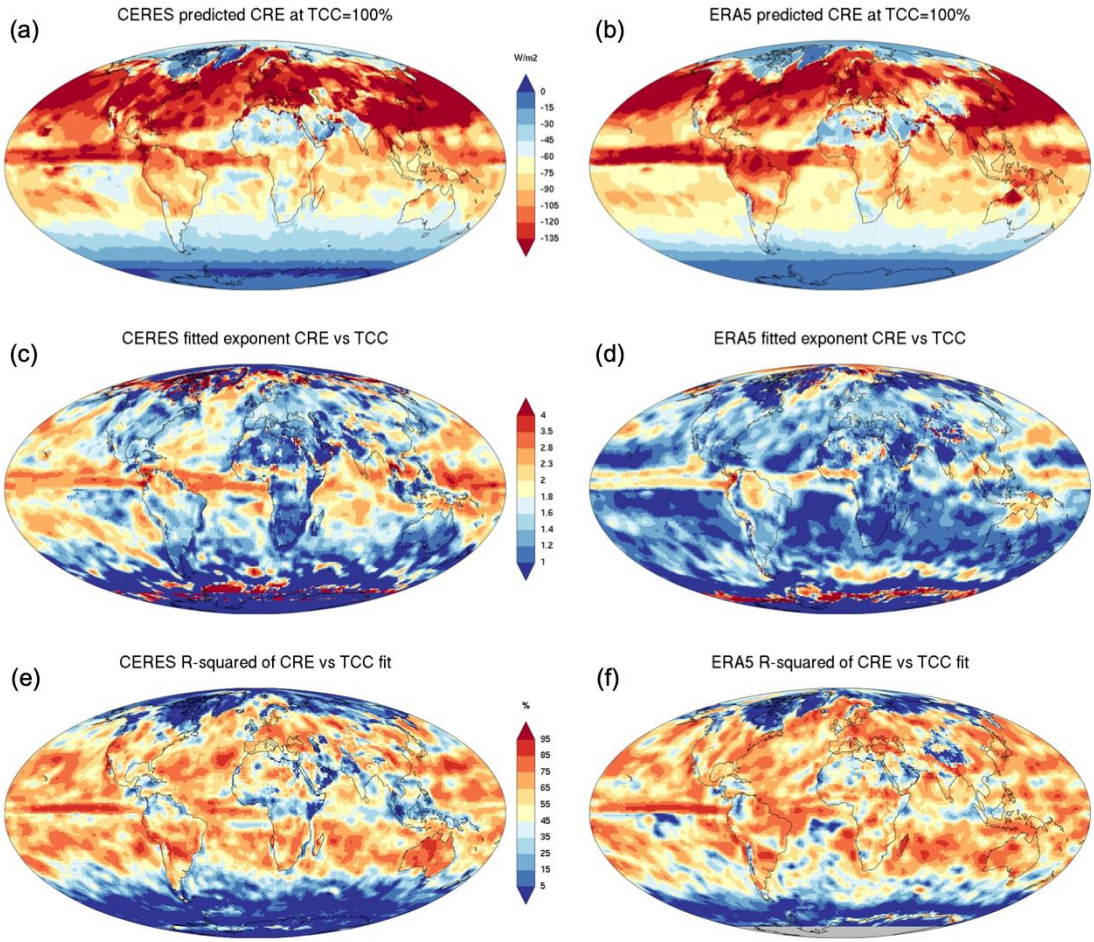


***Fig. S9. Parameters of the power functions fitted to the TCC-CRE-relation for May.*** *Based on inter-annual variations of monthly data 2001–2014, with May chosen arbitrarily as an example. (a) linear coefficient α corresponding to the predicted CRE at TCC=100% based on CERES; (b) same but based on ERA5; (c) exponent β with values above 1 indicating a superlinear dependence of CRE on TCC based on CERES; (d) same but based on ERA5; (e) Fraction of CRE variance explained by the fit based on CERES; (f) same but based on ERA5.*

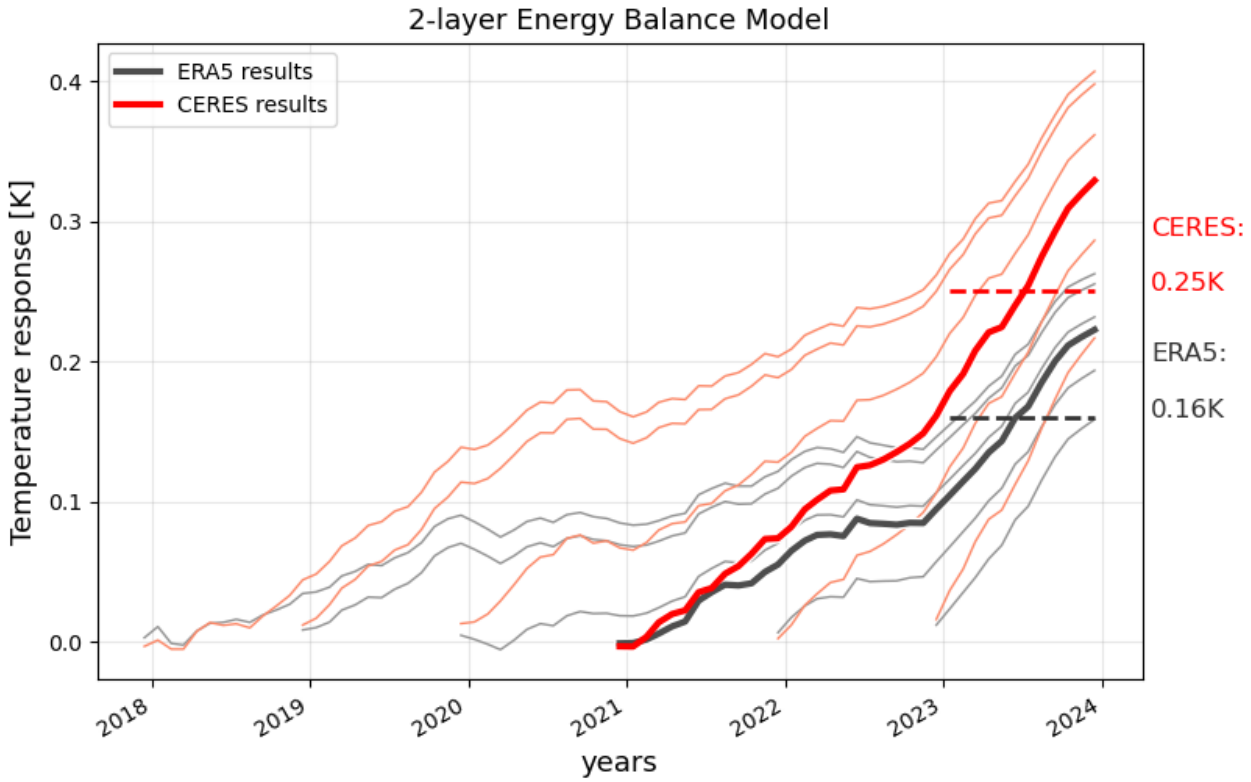


***Fig. S10. Upper-layer temperature response [K] to anomalous absorbed solar radiation from the CERES (red lines) and ERA5 (gray lines) datasets with respect to their 2001-2022 climatology.*** *The temperature estimate is computed with the 2-layer Energy Balance Model. Individual lines are initialized from December 2017 until December 2023, and then the solution to the EBM is found until December 2023. Horizontal dashed lines give the mean temperature response for the whole year 2023 (CERES: 0.25K, in red; ERA5: 0.16K, in black) for solutions initialized in December 2020, respectively.*

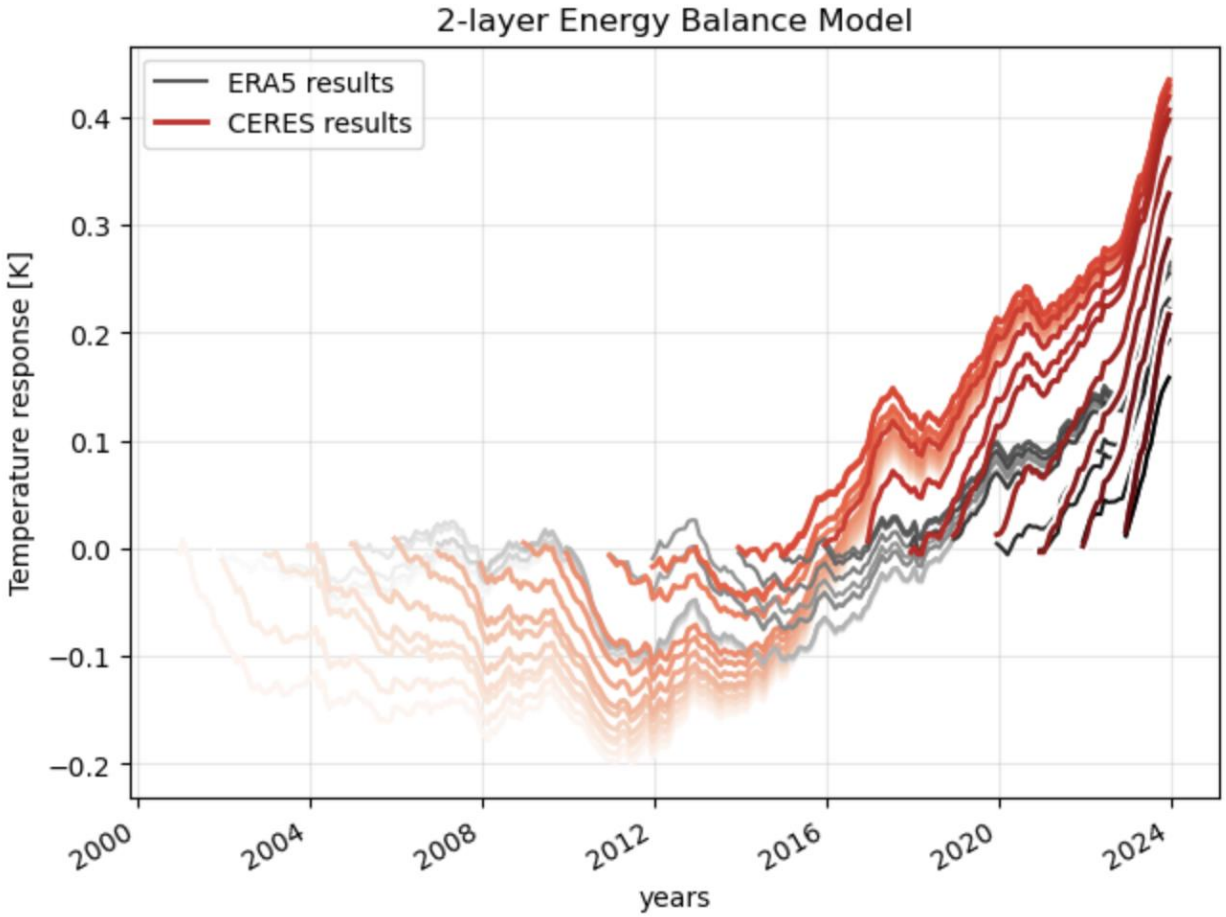


***Fig. S11. Upper-layer temperature response [K] to anomalous absorbed solar radiation from the CERES (red lines) and ERA5 (gray lines) datasets with respect to their 2001-2022 climatology.*** *The temperature estimate is computed with the 2-layer Energy Balance Model. Individual lines are initialized from all Decembers in the period December 2000 to December 2023, and then the solution to the EBM is found until December 2023.*

***Table S1.***

*Parameters used in the 2-layer Energy Balance Model in this study. The parameters follow (42) and (44). By excluding the INM-CM4 model, the fitted ensemble-mean deep-ocean heat capacity $C_0$ has a much smaller standard deviation of 27 W yr $m^{-2}$ $K^{-1}$ (44), indicating that the INM-CM4 might be an outlier in the multi-model CMIP ensemble, and therefore the parameters based on the remaining models are used here.*

| **$F_{eff}$ (forcing efficacy)** | **$\lambda$ (radiative feedback parameter)** | **$\gamma$ (heat exchange coefficient)** | **$C$ (upper heat capacity)** | **$C_0$ (deep-ocean heat capacity)** |
|---|---|---|---|---|
| 0.92<br><br>(*ref 42*) | 1.13 W $m^{-2}$ $K^{-1}$<br><br>(MMM in Table 3 in *ref 44*) | 0.74 W $m^{-2}$ $K^{-1}$<br><br>(MMM in Table 4 in *ref 44*) | 7.3 W yr $m^{-2}$ $K^{-1}$<br><br>(MMM in Table 4 in *ref 44*) | 91.0 W yr $m^{-2}$ $K^{-1}$<br><br>(MMM in Table 4 in *ref 44*) |

**References and Notes**


1. T. Iwakiri, Y. Imada, Y. Takaya, T. Kataoka, H. Tatebe, M. Watanabe, Triple-dip La Niña in 2020–23: North Pacific atmosphere drives 2nd year La Niña. *Geophys. Res. Lett.* **50**, e2023GL105763 (2023). doi:10.1029/2023GL105763

2. Copernicus Climate Change Service (C3S), European State of the Climate 2023, Summary (2024); https://doi.org/10.24381/bs9v-8c66.

3. G. Schmidt, Climate models can't explain 2023's huge heat anomaly - we could be in uncharted territory. *Nature* **627**, 467 (2024). doi:10.1038/d41586-024-00816-z Medline

4. T. Rackow, S. Danilov, H. F. Goessling, H. H. Hellmer, D. V. Sein, T. Semmler, D. Sidorenko, T. Jung, Delayed Antarctic sea-ice decline in high-resolution climate change simulations. *Nat. Commun.* **13**, 637 (2022). doi:10.1038/s41467-022-28259-y Medline

5. T. Kuhlbrodt, R. Swaminathan, P. Ceppi, T. Wilder, A glimpse into the future: The 2023 ocean temperature and sea ice extremes in the context of longer-term climate change. *Bull. Am. Meteorol. Soc.* **105**, E474–E485 (2024). doi:10.1175/BAMS-D-23-0209.1

6. L. A. Roach, W. N. Meier, Sea ice in 2023. *Nat. Rev. Earth Environ.* **5**, 235–237 (2024). doi:10.1038/s43017-024-00542-0

7. G. Kopp, Magnitudes and timescales of total solar irradiance variability. *J. Space Weather Space Clim.* **6**, A30 (2016). doi:10.1051/swsc/2016025

8. M. R. Schoeberl, Y. Wang, G. Taha, D. J. Zawada, R. Ueyama, A. Dessler, Evolution of the climate forcing during the two years after the Hunga Tonga-Hunga Ha'apai eruption. *J. Geophys. Res. Atmos.* **129**, e2024JD041296 (2024). doi:10.1029/2024JD041296

9. J. Hansen, M. Sato, L. Simons, L. S. Nazarenko, I. Sangha, P. Kharecha, J. C. Zachos, K. von Schuckmann, N. G. Loeb, M. B. Osman, Q. Jin, G. Tselioudis, E. Jeong, A. Lacis, R. Ruedy, G. Russell, J. Cao, J. Li, Global warming in the pipeline. *Oxford Open Climate Change* **3**, kgad008 (2024). doi:10.1093/oxfclm/kgad008

10. P. Manshausen, D. Watson-Parris, M. W. Christensen, J. P. Jalkanen, P. Stier, Invisible ship tracks show large cloud sensitivity to aerosol. *Nature* **610**, 101–106 (2022). doi:10.1038/s41586-022-05122-0 Medline

11. Ø. Hodnebrog, G. Myhre, C. Jouan, T. Andrews, P. M. Forster, H. Jia, N. G. Loeb, D. J. L. Olivié, D. Paynter, J. Quaas, S. P. Raghuraman, M. Schulz, Recent reductions in aerosol emissions have increased Earth's energy imbalance. *Commun. Earth Environ.* **5**, 166 (2024). doi:10.1038/s43247-024-01324-8

12. H. Wang, X.-T. Zheng, W. Cai, Z.-W. Han, S.-P. Xie, S. M. Kang, Y.-F. Geng, F. Liu, C.-Y. Wang, Y. Wu, B. Xiang, L. Zhou, Atmosphere teleconnections from abatement of China aerosol emissions exacerbate Northeast Pacific warm blob events. *Proc. Natl. Acad. Sci. U.S.A.* **121**, e2313797121 (2024). doi:10.1073/pnas.2313797121 Medline

13. T. Yuan, H. Song, L. Oreopoulos, R. Wood, H. Bian, K. Breen, M. Chin, H. Yu, D. Barahona, K. Meyer, S. Platnick, Abrupt reduction in shipping emission as an inadvertent geoengineering termination shock produces substantial radiative warming. *Commun. Earth Environ.* **5**, 281 (2024). doi:10.1038/s43247-024-01442-3 Medline

14. N. G. Loeb, D. R. Doelling, H. Wang, W. Su, C. Nguyen, J. G. Corbett, L. Liang, C. Mitrescu, F. G. Rose, S. Kato, Clouds and the Earth's Radiant Energy System (CERES) Energy Balanced and Filled (EBAF) Top-of-Atmosphere (TOA) Edition-4.0 data product. *J. Clim.* **31**, 895–918 (2018). doi:10.1175/JCLI-D-17-0208.1

15. P. Minnis, S. Sun-Mack, Y. Chen, F.-Y. Chang, C. R. Yost, W. L. Smith, "CERES MODIS cloud product retrievals for edition 4—Part I: Algorithm changes" in *IEEE Transactions on Geoscience and Remote Sensing*, vol. 59 (IEEE, 2021); pp. 2744–2780.

16. T. Dudok de Wit, G. Kopp, C. Fröhlich, M. Schöll, Methodology to create a new total solar irradiance record: Making a composite out of multiple data records. *Geophys. Res. Lett.* **44**, 1196–1203 (2017). doi:10.1002/2016GL071866

17. H. Hersbach, B. Bell, P. Berrisford, S. Hirahara, A. Horányi, J. Muñoz-Sabater, J. Nicolas, C. Peubey, R. Radu, D. Schepers, A. Simmons, C. Soci, S. Abdalla, X. Abellan, G. Balsamo, P. Bechtold, G. Biavati, J. Bidlot, M. Bonavita, G. De Chiara, P. Dahlgren, D. Dee, M. Diamantakis, R. Dragani, J. Flemming, R. Forbes, M. Fuentes, A. Geer, L. Haimberger, S. Healy, R. J. Hogan, E. Hólm, M. Janisková, S. Keeley, P. Laloyaux, P. Lopez, C. Lupu, G. Radnoti, P. de Rosnay, I. Rozum, F. Vamborg, S. Villaume, J.-N. Thépaut, The ERA5 global reanalysis. *Q. J. R. Meteorol. Soc.* **146**, 1999–2049 (2020). doi:10.1002/qj.3803

18. B. Bell, H. Hersbach, A. Simmons, P. Berrisford, P. Dahlgren, A. Horányi, J. Muñoz-Sabater, J. Nicolas, R. Radu, D. Schepers, C. Soci, S. Villaume, J.-R. Bidlot, L. Haimberger, J. Woollen, C. Buontempo, J.-N. Thépaut, The ERA5 global reanalysis: Preliminary extension to 1950. *Q. J. R. Meteorol. Soc.* **147**, 4186–4227 (2021). doi:10.1002/qj.4174

19. N. G. Loeb, S.-H. Ham, R. P. Allan, T. J. Thorsen, B. Meyssignac, S. Kato, G. C. Johnson, J. M. Lyman, Observational assessment of changes in Earth's energy imbalance since 2000. *Surv. Geophys.* (2024). doi:10.1007/s10712-024-09838-8

20. H. Song, Y.-S. Choi, H. Kang, Global change in cloud radiative effect revealed in CERES observations. Research Square 10.21203/rs.3.rs-3781529/v1 [Preprint] (2024); https://www.researchsquare.com/article/rs-3781529/v1.

21. N. G. Loeb, G. C. Johnson, T. J. Thorsen, J. M. Lyman, F. G. Rose, S. Kato, Satellite and ocean data reveal marked increase in Earth's heating rate. *Geophys. Res. Lett.* **48**, e2021GL093047 (2021). doi:10.1029/2021GL093047

22. A. Donohoe, K. C. Armour, A. G. Pendergrass, D. S. Battisti, Shortwave and longwave radiative contributions to global warming under increasing $CO_2$. *Proc. Natl. Acad. Sci. U.S.A.* **111**, 16700–16705 (2014). doi:10.1073/pnas.1412190111 Medline

23. Y. He, K. Wang, C. Zhou, M. Wild, A revisit of global dimming and brightening based on the sunshine duration. *Geophys. Res. Lett.* **45**, 4281–4289 (2018). doi:10.1029/2018GL077424

24. S. Kato, Interannual variability of the global radiation budget. *J. Clim.* **22**, 4893–4907 (2009). doi:10.1175/2009JCLI2795.1

25. C. Radley, S. Fueglistaler, L. Donner, Cloud and radiative balance changes in response to ENSO in observations and models. *J. Clim.* **27**, 3100–3113 (2014). doi:10.1175/JCLI-D-13-00338.1

26. G. L. Stephens, D. O'Brien, P. J. Webster, P. Pilewski, S. Kato, J. Li, The albedo of Earth. *Rev. Geophys.* **53**, 141–163 (2015). doi:10.1002/2014RG000449

27. A. Timmermann, S.-I. An, J.-S. Kug, F.-F. Jin, W. Cai, A. Capotondi, K. M. Cobb, M. Lengaigne, M. J. McPhaden, M. F. Stuecker, K. Stein, A. T. Wittenberg, K.-S. Yun, T. Bayr, H.-C. Chen, Y. Chikamoto, B. Dewitte, D. Dommenget, P. Grothe, E. Guilyardi, Y.-G. Ham, M. Hayashi, S. Ineson, D. Kang, S. Kim, W. Kim, J.-Y. Lee, T. Li, J.-J. Luo, S. McGregor, Y. Planton, S. Power, H. Rashid, H.-L. Ren, A. Santoso, K. Takahashi, A. Todd, G. Wang, G. Wang, R. Xie, W.-H. Yang, S.-W. Yeh, J. Yoon, E. Zeller, X. Zhang, El Niño-Southern Oscillation complexity. *Nature* **559**, 535–545 (2018). doi:10.1038/s41586-018-0252-6 Medline

28. B. Huang, P. W. Thorne, V. F. Banzon, T. Boyer, G. Chepurin, J. H. Lawrimore, M. J. Menne, T. M. Smith, R. S. Vose, H.-M. Zhang, Extended Reconstructed Sea Surface Temperature, Version 5 (ERSSTv5): Upgrades, validations, and intercomparisons. *J. Clim.* **30**, 8179–8205 (2017). doi:10.1175/JCLI-D-16-0836.1

29. A. Letterly, J. Key, Y. Liu, Arctic climate: Changes in sea ice extent outweigh changes in snow cover. *Cryosphere* **12**, 3373–3382 (2018). doi:10.5194/tc-12-3373-2018

30. A. Riihelä, R. M. Bright, K. Anttila, Recent strengthening of snow and ice albedo feedback driven by Antarctic sea-ice loss. *Nat. Geosci.* **14**, 832–836 (2021). doi:10.1038/s41561-021-00841-x

31. A. Donohoe, D. S. Battisti, Atmospheric and surface contributions to planetary albedo. *J. Clim.* **24**, 4402–4418 (2011). doi:10.1175/2011JCLI3946.1

32. N. G. Loeb, H. Wang, F. G. Rose, S. Kato, W. L. Smith Jr., S. Sun-Mack, Decomposing shortwave top-of-atmosphere and surface radiative flux variations in terms of surface and atmospheric contributions. *J. Clim.* **32**, 5003–5019 (2019). doi:10.1175/JCLI-D-18-0826.1

33. S. Kato, N. G. Loeb, P. Minnis, J. A. Francis, T. P. Charlock, D. A. Rutan, E. E. Clothiaux, S. Sun-Mack, Seasonal and interannual variations of top-of-atmosphere irradiance and cloud cover over polar regions derived from the CERES data set. *Geophys. Res. Lett.* **33**, L19804 (2006). doi:10.1029/2006GL026685

34. M. D. Zelinka, S. A. Klein, D. L. Hartmann, Computing and partitioning cloud feedbacks using cloud property histograms. Part II: Attribution to changes in cloud amount, altitude, and optical depth. *J. Clim.* **25**, 3736–3754 (2012). doi:10.1175/JCLI-D-11-00249.1

35. S. A. Klein, A. Hall, J. R. Norris, R. Pincus, Low-cloud feedbacks from cloud-controlling factors: A review. *Surv. Geophys.* **38**, 1307–1329 (2017). doi:10.1007/s10712-017-9433-3

36. S. Twomey, The influence of pollution on the shortwave albedo of clouds. *J. Atmos. Sci.* **34**, 1149–1152 (1977). doi:10.1175/1520-0469(1977)034<1149:TIOPOT>2.0.CO;2

37. J. Quaas, B. Stevens, P. Stier, U. Lohmann, Interpreting the cloud cover – aerosol optical depth relationship found in satellite data using a general circulation model. *Atmos. Chem. Phys.* **10**, 6129–6135 (2010). doi:10.5194/acp-10-6129-2010

38. J. Li, B. E. Carlson, Y. L. Yung, D. Lv, J. Hansen, J. E. Penner, H. Liao, V. Ramaswamy, R. A. Kahn, P. Zhang, O. Dubovik, A. Ding, A. A. Lacis, L. Zhang, Y. Dong, Scattering and

absorbing aerosols in the climate system. *Nat. Rev. Earth Environ.* **3**, 363–379 (2022). doi:10.1038/s43017-022-00296-7

39. G. Tselioudis, W. B. Rossow, F. Bender, L. Oreopoulos, J. Remillard, Oceanic cloud trends during the satellite era and their radiative signatures. *Clim. Dyn.* **62**, 9319–9332 (2024). doi:10.1007/s00382-024-07396-8

40. K. E. Taylor, M. Crucifix, P. Braconnot, C. D. Hewitt, C. Doutriaux, A. J. Broccoli, J. F. B. Mitchell, M. J. Webb, Estimating shortwave radiative forcing and response in climate models. *J. Clim.* **20**, 2530–2543 (2007). doi:10.1175/JCLI4143.1

41. M. S. Diamond, Detection of large-scale cloud microphysical changes within a major shipping corridor after implementation of the International Maritime Organization 2020 fuel sulfur regulations. *Atmos. Chem. Phys.* **23**, 8259–8269 (2023). doi:10.5194/acp-23-8259-2023

42. J. Hansen, M. Sato, R. Ruedy, L. Nazarenko, A. Lacis, G. A. Schmidt, G. Russell, I. Aleinov, M. Bauer, S. Bauer, N. Bell, B. Cairns, V. Canuto, M. Chandler, Y. Cheng, A. Del Genio, G. Faluvegi, E. Fleming, A. Friend, T. Hall, C. Jackman, M. Kelley, N. Kiang, D. Koch, J. Lean, J. Lerner, K. Lo, S. Menon, R. Miller, P. Minnis, T. Novakov, V. Oinas, J. Perlwitz, J. Perlwitz, D. Rind, A. Romanou, D. Shindell, P. Stone, S. Sun, N. Tausnev, D. Thresher, B. Wielicki, T. Wong, M. Yao, S. Zhang, Efficacy of climate forcings. *J. Geophys. Res.* **110**, D18104 (2005). doi:10.1029/2005JD005776

43. I. M. Held, M. Winton, K. Takahashi, T. Delworth, F. Zeng, G. K. Vallis, Probing the fast and slow components of global warming by returning abruptly to preindustrial forcing. *J. Clim.* **23**, 2418–2427 (2010). doi:10.1175/2009JCLI3466.1

44. O. Geoffroy, D. Saint-Martin, D. J. L. Olivié, A. Voldoire, G. Bellon, S. Tytéca, Transient climate response in a two-layer energy-balance model. Part I: Analytical solution and parameter calibration using CMIP5 AOGCM experiments. *J. Clim.* **26**, 1841–1857 (2013). doi:10.1175/JCLI-D-12-00195.1

45. M. D. Zelinka, C. Zhou, S. A. Klein, Insights from a refined decomposition of cloud feedbacks. *Geophys. Res. Lett.* **43**, 9259–9269 (2016). doi:10.1002/2016GL069917

46. D. Zanchettin, C. Timmreck, M. Khodri, A. Schmidt, M. Toohey, M. Abe, S. Bekki, J. Cole, S.-W. Fang, W. Feng, G. Hegerl, B. Johnson, N. Lebas, A. N. LeGrande, G. W. Mann, L. Marshall, L. Rieger, A. Robock, S. Rubinetti, K. Tsigaridis, H. Weierbach, Effects of forcing differences and initial conditions on inter-model agreement in the VolMIP volc-pinatubo-full experiment. *Geosci. Model Dev.* **15**, 2265–2292 (2022). doi:10.5194/gmd-15-2265-2022

47. K. Li, F. Zheng, J. Zhu, Q.-C. Zeng, El Niño and the AMO sparked the astonishingly large margin of warming in the global mean surface temperature in 2023. *Adv. Atmos. Sci.* **41**, 1017–1022 (2024). doi:10.1007/s00376-023-3371-4

48. C. L. Boehm, D. W. J. Thompson, The key role of cloud–climate coupling in extratropical sea surface temperature variability. *J. Clim.* **36**, 2753–2762 (2023). doi:10.1175/JCLI-D-22-0362.1

49. M. Athanase, A. Sánchez-Benítez, H. F. Goessling, F. Pithan, T. Jung, Projected amplification of summer marine heatwaves in a warming Northeast Pacific Ocean. *Commun. Earth Environ.* **5**, 53 (2024). doi:10.1038/s43247-024-01212-1

50. X. Qu, A. Hall, S. A. Klein, P. M. Caldwell, On the spread of changes in marine low cloud cover in climate model simulations of the 21st century. *Clim. Dyn.* **42**, 2603–2626 (2014). doi:10.1007/s00382-013-1945-z

51. S. C. Sherwood, M. J. Webb, J. D. Annan, K. C. Armour, P. M. Forster, J. C. Hargreaves, G. Hegerl, S. A. Klein, K. D. Marvel, E. J. Rohling, M. Watanabe, T. Andrews, P. Braconnot, C. S. Bretherton, G. L. Foster, Z. Hausfather, A. S. von der Heydt, R. Knutti, T. Mauritsen, J. R. Norris, C. Proistosescu, M. Rugenstein, G. A. Schmidt, K. B. Tokarska, M. D. Zelinka, An assessment of Earth's climate sensitivity using multiple lines of evidence. *Rev. Geophys.* **58**, RG000678 (2020). doi:10.1029/2019RG000678 Medline

52. C. J. Smith, R. J. Kramer, G. Myhre, K. Alterskjær, W. Collins, A. Sima, O. Boucher, J.-L. Dufresne, P. Nabat, M. Michou, S. Yukimoto, J. Cole, D. Paynter, H. Shiogama, F. M. O'Connor, E. Robertson, A. Wiltshire, T. Andrews, C. Hannay, R. Miller, L. Nazarenko, A. Kirkevåg, D. Olivié, S. Fiedler, A. Lewinschal, C. Mackallah, M. Dix, R. Pincus, P. M. Forster, Effective radiative forcing and adjustments in CMIP6 models. *Atmos. Chem. Phys.* **20**, 9591–9618 (2020). doi:10.5194/acp-20-9591-2020

53. J. T. Kiehl, Twentieth century climate model response and climate sensitivity. *Geophys. Res. Lett.* **34**, L22710 (2007). doi:10.1029/2007GL031383

54. P. M. Forster, T. Andrews, P. Good, J. M. Gregory, L. S. Jackson, M. Zelinka, Evaluating adjusted forcing and model spread for historical and future scenarios in the CMIP5 generation of climate models. *J. Geophys. Res. Atmos.* **118**, 1139–1150 (2013). doi:10.1002/jgrd.50174